Momentum transfer of solar wind plasma in a kinetic scale magnetosphere

Cite as: Phys. Plasmas **19**, 032111 (2012); https://doi.org/10.1063/1.3683560
Submitted: 10 October 2011 • Accepted: 03 January 2012 • Published Online: 23 March 2012

Toseo Moritaka, Yoshihiro Kajimura, Hideyuki Usui, et al.

Momentum transfer of solar wind plasma in a kinetic scale magnetosphere

Toseo Moritaka,[1,2,3,a)] Yoshihiro Kajimura,[3,4] Hideyuki Usui,[2,3] Masaharu Matsumoto,[2,3,4] Tatsuki Matsui,[2,3] and Iku Shinohara[3,4]
[1]*Institute for Laser Engineering, Osaka University, Suita, Osaka 565-0871, Japan*
[2]*Graduate School of System Informatics, Kobe University, Nada, Kobe 657-8501, Japan*
[3]*Japan Science and Technology Agency (JST), CREST, Kawaguchi 332-0012, Japan*
[4]*Institute of Space and Astronautical Science, Japan Aerospace Exploration Agency, Sagamihara, Kanagawa 229-8510, Japan*

(Received 10 October 2011; accepted 3 January 2012; published online 23 March 2012)

Solar wind interaction with a kinetic scale magnetosphere and the resulting momentum transfer process are investigated by 2.5-dimensional full kinetic particle-in-cell simulations. The spatial scale of the considered magnetosphere is less than or comparable to the ion inertial length and is relevant for magnetized asteroids or spacecraft with mini-magnetosphere plasma propulsion. Momentum transfer is evaluated by studying the Lorentz force between solar wind plasma and a hypothetical coil current density that creates the magnetosphere. In the zero interplanetary magnetic field (IMF) limit, solar wind interaction goes into a steady state with constant Lorentz force. The dominant Lorentz force acting on the coil current density is applied by the thin electron current layer at the wind-filled front of the magnetosphere. Dynamic pressure of the solar wind balances the magnetic pressure in this region via electrostatic deceleration of ions. The resulting Lorentz force is characterized as a function of the scale of magnetosphere normalized by the electron gyration radius, which determines the local structure of the current layer. For the finite northward IMF case, solar wind electrons flow into the magnetosphere through the reconnecting region. The inner electrons enhance the ion deceleration, and this results in temporal increment of the Lorentz force. It is concluded that the momentum transfer of solar wind plasma could take place actively with variety of kinetic plasma phenomena, even in a magnetosphere with a small scale of less than the ion inertial length. © *2012 American Institute of Physics*.
[doi:10.1063/1.3683560]

I. INTRODUCTION

The geomagnetosphere has been studied in collisionless plasma physics for a number of years in terms of both its global structure from a macroscopic viewpoint and local kinetic phenomena from a microscopic viewpoint.[1] In addition, considerable knowledge about the magnetospheres of other magnetized objects, such as Mercury,[2] Jupiter,[3] Ganymede,[4,5] and magnetized asteroids, have been acquired from satellite observations. Understanding magnetospheres with various scale lengths and solar wind conditions provides a universal framework for solar wind interaction, especially when studying the relationship between the global structure and local kinetic phenomena of magnetospheres.

To investigate the role of ion-scale kinetic phenomena in global solar wind interaction, a series of hybrid (kinetic ion, fluid electron) particle-in-cell (PIC) simulations have been performed by Omidi *et al.*[6,7] and Blanco-Cano *et al.*[13] As a result of these simulations, scale size dependence of solar wind interaction was demonstrated in the formation of bow shocks, bow waves, and wake structures.[6,7] The formation of these structures is characterized by the magnetosphere scale, L, normalized by ion inertia length, S_i. Large magnetospheres at a scale of $L \geq 20S_i$ have fundamentally the same structure as the geomagnetosphere, whereas for small magnetospheres at a scale of $L \leq 0.2S_i$, no evidence of solar wind interaction has been found, but the existence of whistler wake has been indicated.[8–10] Similarities observed in planetary magnetospheres for various interplanetary magnetic field (IMF) conditions were successfully demonstrated in the simulations.[11–13] For a small-scale magnetosphere, comparable to the ion inertial length or less, differentiation from the geomagnetosphere due to ion kinetic effects would be evident. However, there are few precise observations in the solar system for comparison with the simulations.

Small-scale magnetospheres have also been considered in relation to technological application of solar wind interaction to spacecraft propulsion systems. In a next-generation interplanetary flight system called a magnetic sail,[14] an artificial magnetosphere is created by a hoop coil inside the spacecraft. A propulsive force is generated from the reactive force to scattering of the solar wind plasma at the front of the magnetosphere. To enlarge the scatter surface, in the mini-magnetosphere plasma propulsion approach (M2P2) (Ref. 17), magnetic inflation by plasma injection[15,16] is considered. The primary benefit of these systems is their fuel efficiency when compared with chemical propulsion. Solar wind scattering is produced by electromagnetic interaction between the magnetosphere and collisionless plasma. Therefore, quantitative estimation of the propulsion obtained is not straightforward. Moreover, the size of magnetosphere generated by a practical coil is expected to be a few hundred

[a)]Electronic mail: moritaka-t@ile.osaka-u.ac.jp.

meters, considerably less than the ion inertial length. For these systems, the kinetic effects of electrons, in addition to ions, could play a role in the interaction process, in a manner that is different to effects appearing in planetary magnetospheres.

A number of magnetohydrodynamics (MHD),[18] two-fluid,[17] and hybrid PIC[19–22] simulations have been performed in order to investigate the solar wind interaction in an artificial magnetosphere and the evaluation of the propulsion. In MHD simulations assuming zero IMF,[18] solar wind plasma is reflected completely at the front of the magnetosphere, and the resulting propulsion is proportional to the cross section of the magnetosphere. The propulsion computed by the MHD simulation is represented as a scale-independent drag coefficient. Here, the drag coefficient is a characteristic parameter indicating propulsion and is defined as the propulsive force normalized by the product of dynamic pressure and characteristic section area.

Scale dependence of the drag coefficient is reported in hybrid simulations[20,22] for a severe reduction in an ion-scale magnetosphere $L \leq S_i$. The reduction is construed as originating from penetration of solar wind ions into the magnetosphere and attributed to the ion's inertia. Conversely, a pressure balance between solar wind dynamic pressure and the magnetic field is confirmed at the front of the magnetosphere, even for $L \sim S_i$,[23] and indicates specular reflection of solar wind plasma. In addition, IMF is assumed to be zero in the drag coefficient simulations.[18,20,22] Clarification of the detailed physics in the magnetospheric boundary, where the magnetosphere interacts with both solar wind plasma and IMF, and their impact on the momentum transfer process would be open to an investigation that includes the electron kinetics missing in previous simulations.

A demonstration space mission for the magnetic sail and M2P2 has been planned.[24] In this mission, a demonstration satellite will be launched into Earth's orbit, and solar wind conditions and propulsive force will be observed. The obtained data are expected to provide important insights about solar wind interaction in a kinetic scale magnetosphere, which has not been observed in astronomical objects. Therefore, the mission and theoretical evaluation of propulsion will make a significant contribution to basic plasma physics, in addition to space aeronautics.

In the present study, solar wind interaction processes in kinetic scale magnetosphere with $L \leq S_i$ are investigated with a 2.5-dimensional full kinetic simulation. The magnetosphere is created by supplying a modeled coil with current throughout the simulation domain. The Lorentz force acting on the coil current density and their scale dependency are evaluated from the simulation results. Because the Lorentz force corresponds to the reaction of solar wind scattering, the Lorentz force characterizes the momentum transfer process. The influence of IMF on momentum transfer is also considered by comparing the simulation results under conditions of zero and finite IMF.

The remainder of this manuscript is organized as follows. In Sec. II, the simulation model used in this study is presented along with validation of the model. Simulation results under the zero IMF condition are shown in Sec. III, and the physical processes that determine the momentum transfer are considered. In Sec. IV, the influence of IMF is discussed, based on simulation results under finite IMF conditions. Finally, conclusions are summarized in Sec. V.

II. SIMULATION MODEL

The present simulation is performed based on a 2.5-dimensional full kinetic electromagnetic PIC simulation code. Time evolution of the plasma and electromagnetic fields are calculated by solving the Newton-Lorentz and Maxwell equations, respectively. The second-order shape factor of a super particle is employed for force calculations and charge accumulation. In addition, the electrostatic component of the electric field is corrected by a Boris-Buneman scheme, such that it satisfies Gauss's law.

For initial equilibrium, a uniform neutral plasma with uniform flow velocity in +x direction and temperature is employed, and the velocity distribution is given by the shifted Maxwell distribution function. Antiparallel current density in the out-of-plane direction is gradually supplied at the center of the simulation domain in the first phase of the time evolution. This current density corresponds to a modeled coil current and creates a magnetosphere. Schematic diagram of the simulation domain is shown in Fig. 1. The spatial profile of the coil current density $\mathrm{J}_z^c(x,y)$ is defined by typical scale L_c and value J^0 as

$$\mathrm{J}_z^c(x,y) = \mathrm{J}^0 \left(\frac{x}{L_c}\right)^3 \exp\left(-\left(\frac{x}{L_c}\right)^2 - \left(\frac{y}{L_c/2}\right)^2\right). \quad (1)$$

$\mathrm{J}_z^c(x,y)$ is added to the current density of the super particles and a resultant dipole-like magnetic field is generated according to the Maxwell equations. Flowing plasma does not directly make contact with the coil but has a force imparted on it by the generated magnetic field. The specific magnetic field generated by only the coil current density in a vacuum is referred to hereafter as the "original magnetosphere." In the case of finite IMF, uniform background magnetic field in the $+y$ direction is utilized.

The Lorentz force in the x direction, F_x^p, acting on coil current density is evaluated. For a general magnetized object, the coil current density can be interpreted as a hypothetical current density that is consistent with the magnetosphere. The drag coefficient, C_d, is defined as

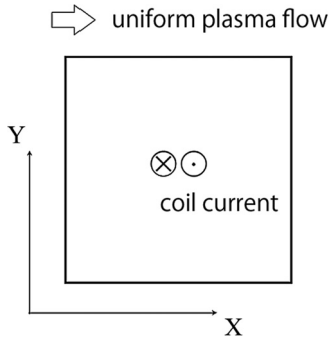

FIG. 1. Schematic diagram of simulation domain. Antiparallel current density is supplied at the center of the domain. Solar wind is assumed to be a uniform plasma flow in the $+x$ direction.

$$C_d = \frac{F_x^p}{P_d S}, \quad P_d = \frac{1}{2} m_i n_i v_{sw}, \tag{2}$$

where P_d, n_i, and v_{sw} are the dynamic pressure, the upstream ion number density, and flow velocity of the plasma, respectively. Here, the typical surface of the two dimensional original magnetosphere, S, is set as $2L$, where L denotes the typical size of the magnetosphere defined as the distance between the coil center and the position where the magnetic pressure of the original magnetosphere is equal to the dynamic pressure.

The electromagnetic field has fixed boundary conditions for the upstream $(-x)$ and $\pm y$ boundaries, and a numerical damping region is placed near these boundaries. Furthermore, a constraint of zero normal derivative is placed on the electromagnetic field at the downstream boundary $(+x)$. To handle continuous plasma inflow and outflow through the simulation boundaries, open boundary conditions[25] are employed for the super particles.

A. Simulation parameters

Three series of parameterizations (series A, B, and C) are performed in order to examine the scale dependence of the solar wind interaction process. The simulation domain is typically implemented on a uniform (1928×1627) point grid. The grid separation and time step interval are set as $\Delta x = \Delta y = 0.31\lambda_D$ and $c\Delta t = 0.5\Delta x$, respectively. Here, λ_D and c are Debye length and light speed, respectively. 32 particles per cell, which is equivalent to $\sim$320 particles per Debye shell, are used for the initial uniform plasma.

In series A, the spatial size of the original magnetosphere is varied while the physical parameters of the solar wind are fixed. The principal dimensionless parameters fixed for the solar wind are the ion-electron mass ratio, $m_i/m_e = 25$, the temperature ratio, $T_i/T_e = 1$, and the flow velocity of solar wind normalized by the ion thermal velocity, $v_{sw}/v_{ti} = 4$. Normalized by the ion inertial length, the spatial size of magnetosphere is varied between $L/S_i = 0.094$ and $L/S_i = 3.5$.

For the other two series, we focus on the characteristic scales of solar wind and fix the size of the magnetosphere. In series B, the ion mass is changed, and the corresponding mass ratio is varied between $m_i/m_e = 25$ and $m_i/m_e = 450$. Accordingly, the spatial size of magnetosphere normalized by ion inertial length changes from $L/S_i = 0.20$ up to $L/S_i = 0.85$, whereas that normalized by the electron inertial length, S_e, is fixed at $L/S_e = 4.3$. In addition, the flow velocity is varied according to the ion mass such that an Alfven Mach number of $v_{sw}/v_a = 2$ is maintained, where v_a denotes the Alfven velocity for unit magnetic field B_0 and the upstream ion number density. The magnetic field B_b balanced by the dynamics pressure is determined by the Alfven Mach number as $B_b/B_0 = v_{sw}/v_a$. Therefore, the expected magnetic field B^b and scale length of the original magnetosphere L are fixed in series B. In series C, the mass ratio is varied between $m_i/m_e = 25$ and $m_i/m_e = 450$ according to the electron mass. As a result, L/S_e changes from 1.0 up to $L/S_e = 4.26$, whereas L/S_i is fixed at 0.20. v_{sw} is also fixed such that $v_{sw}/v_a = 2$ is maintained as in series B.

B. Validation of simulation model

Validation of the simulation model was performed by using test calculations. The width of the simulation domain, X_L, employed in the simulation runs that are discussed in the following chapters is greater than or approximately equal to that used in the test calculation, $X_L/L = 15.7$, which is equivalent to $X_L/S_i = 4.19$. Thus, artifacts resulting from the simulation boundary in the practical simulations are expected to be comparable to, or less than, those found here.

The validation is done from two perspectives. First is the dependence of the total Lorentz force acting on the coil current on the size of the simulation domain and the standoff time of coil current density. Under the influence of solar wind flowing in the $+x$ direction, the magnetosphere becomes asymmetric and the total Lorentz force is expected to have a finite value toward the downstream direction. The time evolution of total Lorentz force is shown as a solid line in Fig. 2(a), where the Lorentz force is normalized by the symmetric repulsion between the $\pm$ components of the coil current density. The dashed and dotted lines in the figure are for an enlarged simulation domain, $X_L/L = 18.4$, and for a

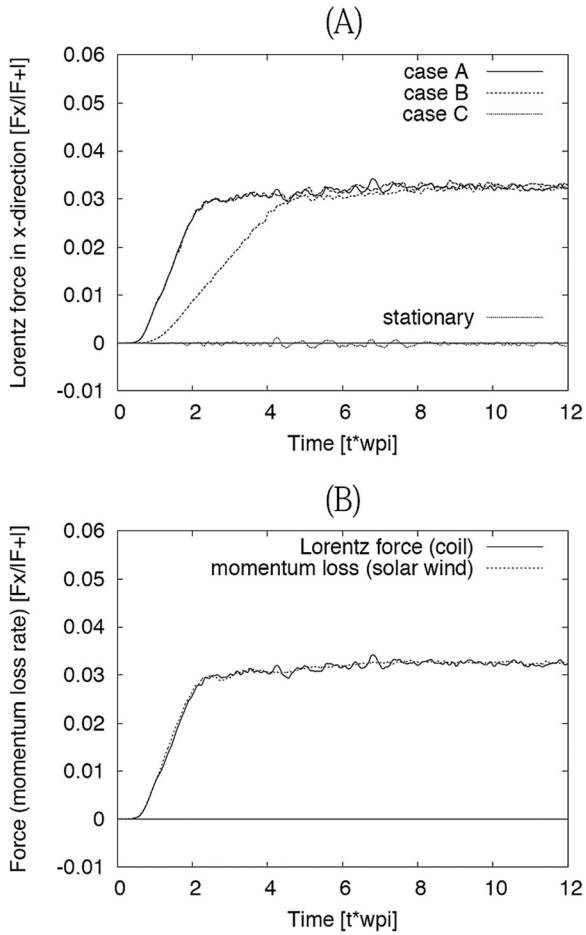

FIG. 2. Time evolutions of Lorentz force acting on coil current density. (a) Dependence on domain size, standoff time, and solar wind flow velocity. Domain size for case B (dashed line) is enlarged compared with that in case A (solid line). The standoff time for case C (dotted line) is twice that for case A. Solar wind flow velocity is set equal to zero for the "stationary" case (dashed-dotted line). (b) Relationship between Lorentz force (solid line) and the momentum loss rate of the solar wind plasma (dashed line).

doubled standoff time, respectively. The resulting Lorentz forces under these conditions are almost identical in the quasi-steady state. In addition, the dashed-dotted line marked as "stationary" in Fig. 2(a) represents the Lorentz force obtained in a stationary solar wind, $v_{sw} = 0$. For this case, the Lorentz force is negligible, having a small fluctuation of $\sim 1\%$ of the Lorentz force obtained under the other conditions. These results suggest that the asymmetry of the Lorentz force in the x-direction originate from neither an artifact of the boundary conditions nor a temporary reaction to the initial rise of the current density.

Second is the action-reaction law that must be satisfied by the solar wind interaction. Figure 2(b) shows time evolutions for the Lorentz force acting on the coil current (solid line) and for the deceleration of solar wind plasma (dashed line). Deceleration is calculated as the summation of the time variation of the relativistic momentum $-d(\gamma mv)/dt$ for all super particles in the simulation domain. These two time evolutions are nearly identical, and the Lorentz force resulting from the simulation can be regarded as a characteristic parameter for the momentum transfer process of solar wind.

III. RESULTS UNDER ZERO INTERPLANETARY MAGNETIC FIELD LIMIT

A. General solar wind interaction

Figure 3 shows typical results from the solar wind interaction process, where the primary parameter values for this example are listed as Case A0 in Table I. In Fig. 3, the mass density, ρ, the out-of-plane current density, J_z, and the out-of-plane magnetic field, B_z, are displayed as color-coded contour plots in (a), (b), and (c), respectively, and the green lines depict the magnetic field lines. The time evolution of the drag coefficient is shown in Fig. 4. The resulting drag coefficient is almost constant when $t\omega_{pi} > 10.0$. The fields shown in Fig. 3 were obtained by averaging over a time period of $28.6 \leq t\omega_{pi} \leq 29.3$ and can be regarded as being in a quasi-steady state.

It is clear from Fig. 3(a) that the solar wind plasma is effectively stagnant at the front of the magnetosphere, even for the small scale magnetosphere with $L = 0.2S_i$. The solar wind interaction results in two types of current density structures. One is a thin out-of-plane current density that is generated at the boundary of the magnetosphere, as shown in Fig. 3(b), and the second is the in-plane loop current density that creates the out-of-plane magnetic field around the magnetosphere. From Fig. 3(c), the resultant magnetic fields are of large scale comparable to the ion inertial length S_i.

At the periphery of the magnetosphere, electron flow is distorted by the magnetic field whereas ions tend to flow smoothly. The loop current density originates from the relative streaming between these electrons and ions, specifically, from a two-fluid effect characterized by the ion inertial length. The loop current density is considered to be relevant to whistler wake without density perturbation that has been observed in previous hybrid simulations.[6] The loop current density does not contribute to the Lorentz force, since the resulting magnetic field is parallel to the coil current density. This result appears consistent with past results showing that almost no solar wind momentum is transferred in an ion scale magnetosphere in which only whistler wake is expected.[7,22] However, the thin layer of out-of-plane current density is generated even in such a small scale magnetosphere and exerts Lorentz force to the coil current.

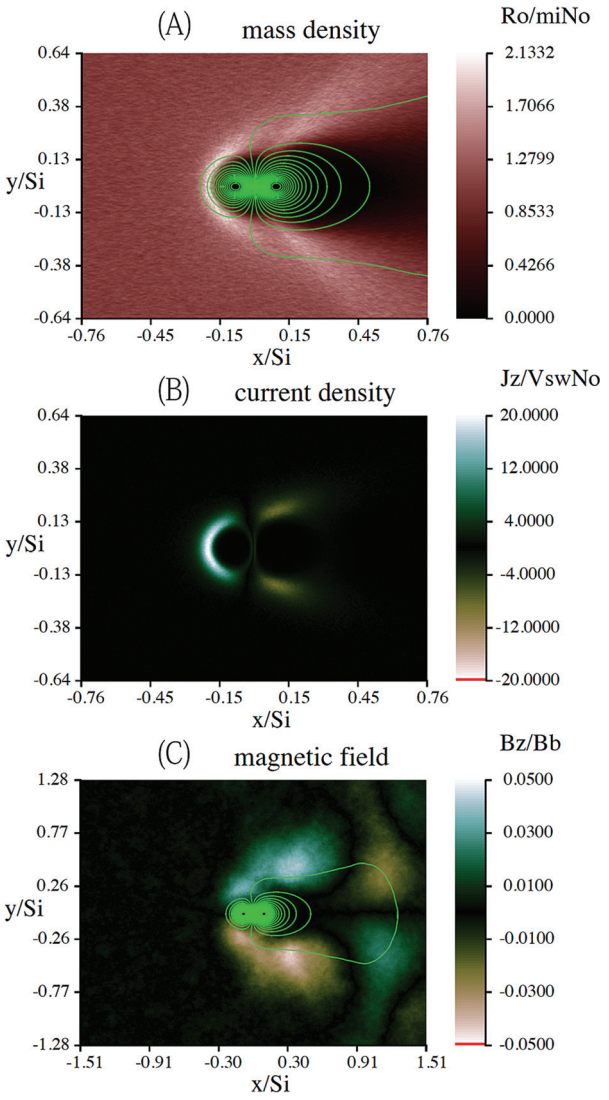

FIG. 3. (Color) Color-coded contour plots of (a) mass density Ro, (b) out-of-plane current density J_z and (c) out-of-plane magnetic field B_z in a quasi-steady state. Green lines represent magnetic field lines. Note: the displayed region is larger in (c) than in (a) and (b).

TABLE I. Dimensionless parameters for simulation series A (A1–A7) and the additional example A0.

Run	L/S_i	L/S_e	m_i/m_e	v_{sw}/v_{ti}	v_{sw}/V_a
A0	0.20	4.26	450	4	2
A1	3.536	17.68	25	4	2
A2	2.656	13.28	25	4	2
A3	1.782	8.91	25	4	2
A4	0.852	4.26	25	4	2
A5	0.41	2.05	25	4	2
A6	0.196	0.98	25	4	2
A7	0.094	0.47	25	4	2

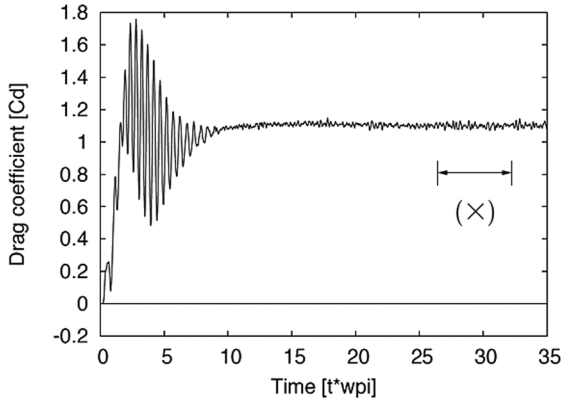

FIG. 4. Time evolution of drag coefficient. Interval marked by "(×)" is used for time averaging the results shown in Fig. 5.

Figure 5(a) shows profiles for steady state magnetic field B_y (dashed line), the original magnetosphere B_y(orig) (dotted line), and the induced out-of-plane current density, dJ_z (solid line), along equatorial line $y = 0$ of the upstream side $x < 0$. Here, B_y and J_z are for the steady state and obtained by averaging in the time period marked as (X) in Fig. 4. The magnetosphere is compressed by solar wind flowing from the $-x$ direction, and a region with steep gradient is formed at the front of the magnetosphere $x \sim -0.2S_i$. The out-of-plane current density is induced at this region. In the steady state, the induced current density and the compressed magnetic field are related to each other according to the Ampere law

$$\frac{dB_y^{orig} + d(dB_y)}{dx} - \frac{dB_x^{orig} + d(dB_x)}{dy} = \frac{4\pi}{c}(J_z^{coil} + dJ_z).$$

Here, the magnetic fields and current density are separated into induced and original components as $B_x = B_x^{orig} + dB_x$, $B_y = B_y^{orig} + dB_y$, and $J_z = J^{coil} + dJ_z$, respectively. Figure 5(b) shows the profiles of these separated components in the same normalization by B_0/S_i. As shown in Fig. 5(b), dB_y/dx (dashed line) increases as a result of the compression of magnetosphere and the increment corresponds to the induced current density, dJ_z (solid line). It is also shown that $-dB_x/dy$ (dotted line) is small compared with the other terms dB_y/dx (dashed line) and its contribution to the induced current density is limited. In addition, the normalized magnetic field at the front region of the magnetosphere is $B_y/B_0 \sim 2$, nearly identical to that expected from the pressure balance $B^b/B_0 = v_{sw}/v_a = 2$. Hence, the dynamic pressure from the solar wind is received by even a small magnetosphere on the scale of $L \sim 0.2S_i$.

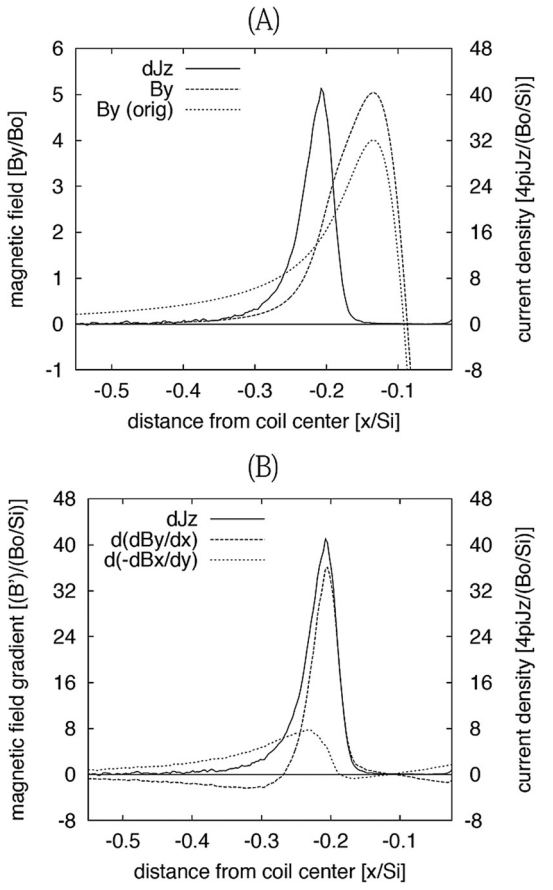

FIG. 5. (a) Profiles of magnetic field, B_y, at steady state (dashed line) and for original magnetosphere, B_y(orig), (dotted line) along the equatorial line ($y = 0$). Profile of induced current density, dJ_z, is also shown as the solid line. (b) Relationship between the induced current, dJ_z, (solid line) and variations of the magnetic field gradient terms, $d(dB_x)/dy$ and $d(dB_y/dx)$ (dotted and dashed lines, respectively).

B. Dependence on spatial scale of magnetosphere

To examine scale dependence of the solar wind interaction, series A of the simulations is run, where the spatial scale of original magnetosphere is varied, while the physical parameters of solar wind are fixed. The principal parameter values used here are summarized in Table I (A1 − A7).

Figure 6 shows profiles for the magnetic field gradient, dB_y/dx (panel a), and induced current density, dJ_z (panel b), for runs A1–A7 in the steady state. The current density peaks in every runs are located near the expected magnetospheric boundary $x \sim -L$, as shown in Fig. 6(b), and magnetic fields are roughly identical to B_b as in run A0.

As shown in Fig. 6(a), the magnetic field gradient increases to a common value for cases with a larger magnetosphere (runs A1–A4). That is, the magnetic field gradient is also determined independently of L. The peak values of induced current density relate to the common value of magnetic field gradient

$$dJ_z = \frac{c}{4\pi} B_b(1/\epsilon_p - 1/\epsilon_B), \tag{3}$$

$$\epsilon_p \equiv \frac{B_b}{(dB_y/dx)}, \quad \epsilon_B \equiv \frac{B_b}{(dB_y^{orig}/dx)},$$

where ϵ_B and ϵ_p are gradient scales of steady state magnetic field, $B_y(\sim B^b)$, and original magnetic field, B_y^{orig}, at the front region of the magnetosphere, respectively. The relationship $dB_x^{orig}/dy - dB_y^{orig}/dx = 0$ that must be satisfied away from the coil center is used here. Because ϵ_p and B_b are independent of L for the case when $\epsilon_B > \epsilon_p$ (runs A1–A4, referred to as the "large magnetosphere regime"), scale dependence of the induced current value is determined by ϵ_B. In the present cases, as shown in Fig. 6(a), the common value of the

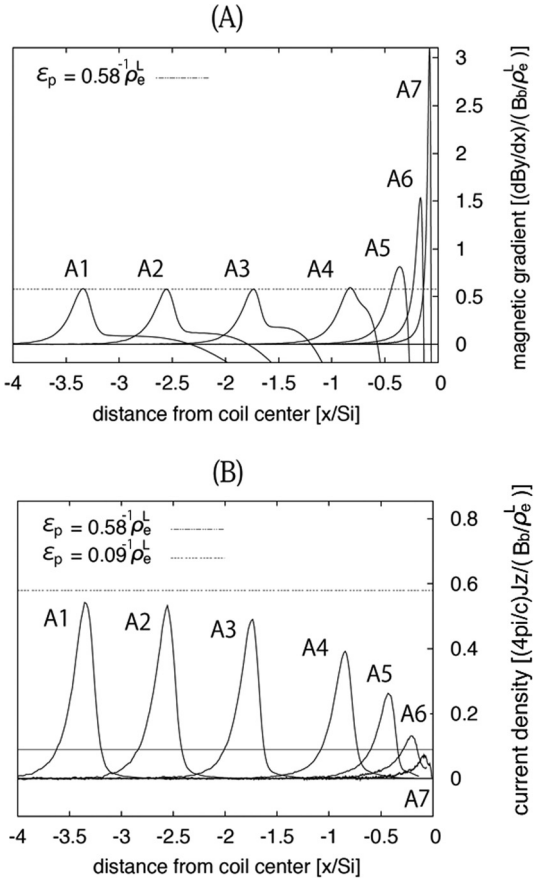

FIG. 6. (a) Profiles of magnetic field gradient, B_y/dx, at steady state for runs A1–A7. For comparison, the magnetic field gradient corresponding to the gradient scale $\epsilon_p = 0.58^{-1}\rho_e^L$ is represented by the dashed line. (b) Profiles of induced current density at steady state for runs A1–A7. The current density values corresponding to the gradient scale $\epsilon_p = 0.58^{-1}\rho_e^L$ and $\epsilon_p = 0.09^{-1}\rho_e^L$ are also shown.

magnetic field gradient is roughly $dBy/dx \sim 0.58B_b/\rho_e^L$, which is equivalent to $\epsilon_p \sim 0.58^{-1}\rho_e^L$, where ρ_e^L is the local electron gyration radius estimated for B_b and estimated mean velocity $v_e^{ave} \equiv \sqrt{(v_{sw}^2 + 2v_{te}^2)}$. Here v_{Te} is the electron thermal velocity for upstream plasma.

Furthermore, a limit value of induced current density can be defined as

$$dJ_z \to \frac{c}{4\pi}\frac{B_b}{\epsilon_p} \equiv dJ_z^{\infty}, \text{ for } L \to \infty, \tag{4}$$

because $\epsilon_B \to 0$ for $L \to \infty$. The limit value of current density is represented by the uppermost horizontal line in Fig. 6(b). When the scale size of the magnetosphere is large, the peak value of current density approaches the limit value.

On the other hand, a small but finite current density is induced even for the small original magnetosphere with a steep field gradient $\epsilon_B < \epsilon_p$ (runs A5–A7, referred to as the "small magnetosphere regime"). As a result, the gradient scale in the steady states exceeds the constant ϵ_p. The induced current density in this regime will be considered in the Force Balance at Magnetospheric Boundary section.

Figure 7 shows the half-width, W_c, of the induced current layer as a function of L. Points "+" and "×" denote the half-width normalized by L and by ρ_e^L, respectively. As seen

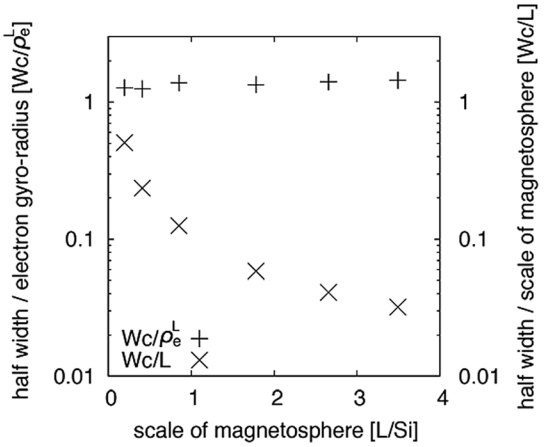

FIG. 7. Dependence of half-width of current layer on the scale of original magnetosphere. Half-widths normalized by the local electron gyration radius and by the scale of magnetosphere are denoted by + and ×, respectively.

in Fig. 7, W_c/ρ_e^L is almost constant, whereas W_c/L decreases according to the increment of L. Explicitly, the half-width of the current layer is comparable with the electron gyration radius, $W_c \sim \rho_e^L$, regardless of the size of the original magnetosphere.

C. Force balance at magnetospheric boundary

To examine the origin of the induced current density, the force balance of solar wind plasma as expressed by the two-fluid equation for steady states $\partial/\partial t = 0$

$$m_j n_j(\mathbf{v}_j \cdot \nabla \mathbf{v}_j) + \nabla \cdot \mathbf{P} = q_j n_j(\mathbf{E} + \mathbf{v}_j \times \mathbf{B}) \tag{5}$$

is evaluated, where m_j, q_j, $\mathbf{v}_j$, and $\mathbf{P}_j$ denote mass, charge, velocity, and pressure tensor for particle species j(=i,e), respectively. Figures 8(a) and 8(c) show profiles for each term in Eq. (5) in the x-direction along equatorial line $y = 0$ for run A4. The magnetic force term $q_j n_j v_{zj} B_y$ relates to the out-of-plane current density. For electrons (Fig. 8(a)), the magnetic force term (red line) balances with the combination of the terms for electric force, $q_e n_e E_x$ (green line), and scalar pressure, $\nabla p_e|_x$ (blue line).

Conversely, the magnetic force term is negligible for ions (Fig. 8(c)). Therefore, the induced current density predominantly consists of the electron current. The electric force for ions is equivalent to that for electrons and balanced dominantly by the pressure terms, indicating that ion momentum toward the downstream direction ($+x$) is dissipated by electrostatic deceleration due to charge separation. The resulting momentum loss of ions relates to the out-of-plane electron current density via the electrostatic interaction, namely,

$$q_e n_e \mathbf{v}_e \times \mathbf{B}|_x \sim \nabla p_e|_x - q_e n_e E_x|_x \sim \nabla(p_i + p_e)|_x.$$

This relationship is consistent with the pressure balance obtained at the front of the magnetosphere.

Electron force balances in the x-direction for various scale size L (runs A3–A7) of original magnetosphere are shown in Fig. 9(a). It can be seen from this figure that the composition of kinetic (dashed lines) and electric terms

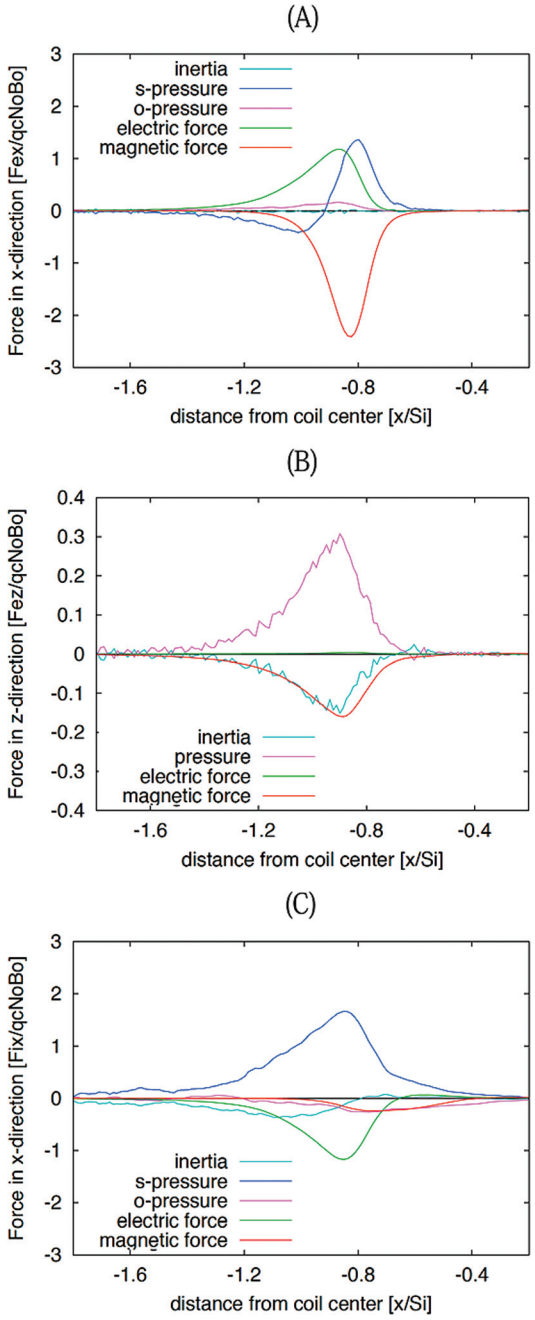

FIG. 8. (Color) Profiles of force terms in the two-fluid equation. Electron force terms in (a) x-direction and (b) z-direction. (c) Ion force terms in the x-direction. Cyan, green, and red lines stand for inertia, electric, and magnetic force terms along equatorial line, respectively. The pressure term is separated into scalar (blue lines) and off-diagonal (purple lines) components for panels (a) and (c).

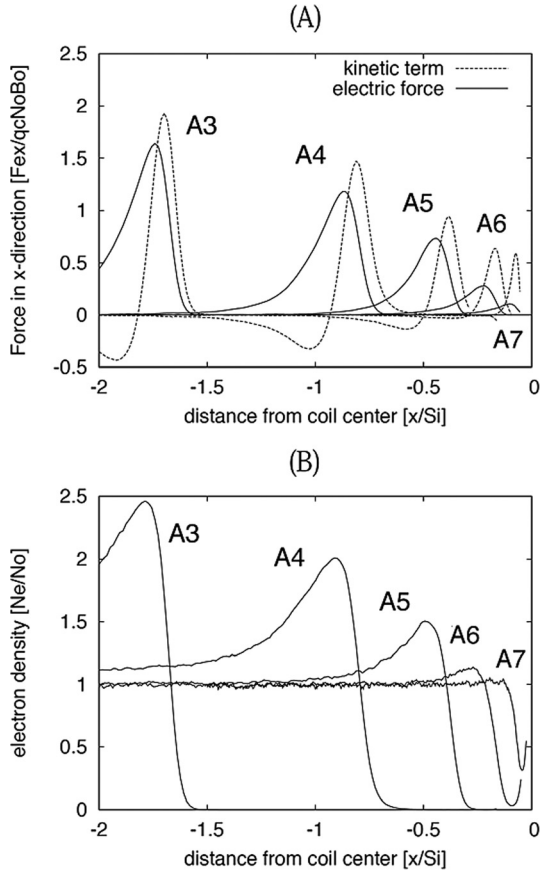

FIG. 9. (a) Profiles of electron force terms from Eq. (5) at steady state for runs A3–A7. Solid and dashed lines denote electric force term and kinetic term including inertia and pressure terms, respectively. (b) Electron number density profiles along equatorial line for runs A3–A7.

(solid lines) in the force balance varies according to the scale of the original magnetosphere. The kinetic term includes scalar pressure and inertia terms. The former mainly contributes this term. When the original magnetosphere is small, the contribution from the electric force term is moderate and the scalar pressure term alone balances the magnetic force term. Figure 9(b) shows the electron number density profiles for each run. Corresponding to decrement of electric force term, the electron pile-up region at the front of the magnetosphere tends to vanish. Therefore, typical values for the current density in the small magnetosphere regime, dJ_z^s, can be evaluated from

$$dJ_z^s \sim \frac{1}{q_e B_b}\frac{p_e}{W_c} \sim \left(\frac{v_{ave}}{v_{sw}}\right)^2 \frac{m_e}{m_i + m_e} dJ_z^\infty, \tag{6}$$

where a half-width of current layer $W_c \sim \rho_e^L$ is assumed and p_e is estimated from the electron mean velocity v_{ave}. This typical value of current density, which is $\sim m_e/m_i$ times smaller than the large limit value, dJ_z^∞, may be relevant to the scattering of solar wind electrons. In the present cases, $(v_{ave}/v_{sw})^2 = 4$ and the corresponding value of dJ_z^s are shown in Fig. 6(b) as the lowermost horizontal line. In the small magnetosphere cases with $\epsilon_B < \epsilon_p$ (runs A6 and A7), the peak values of induced current density is roughly close to the typical value dJ_z^s.

Force balance in the z-direction provides additional information about the induced current density. In the present 2.5-dimensional simulation $\partial/\partial z = 0$, the pressure term $\nabla \cdot \mathbf{P}$ in z-direction originates from the off-diagonal component of the pressure tensor. Figure 8(b) shows the profiles of each electron force term in the z-direction. The inertial term $m_j n_j (\mathbf{v}_j \cdot \nabla \mathbf{v}_j)$ (cyan line), the magnetic force term $\sim n_j q_j v_x B_y$ (red line), and the pressure term $\partial P_{xy}/\partial x$ (purple line) are dominant in the vicinity of the front of the magnetosphere $x \sim L(\sim 0.85 S_i)$. In the present case, each force term is evaluated as follows. In the compression process of magnetosphere, a positive single-layered current density equivalent to $v_{ez} < 0$ is generated. The inertia term becomes

negative in this region, since $v_{ex} > 0$ in solar wind and $v_{ez} = 0$ in the upstream. The magnetic force term is also negative on the upstream side ($B_y > 0$), while the electric force term should be zero in steady states ($E_z = 0$). Therefore, an additional term—the pressure term, $\partial P_{xy}/\partial x$—must have a finite value. The dominance of the pressure term associated with the off-diagonal component indicates the finite orbit effect of the electrons. This suggests the physical origin of the thin current layer having a scale characterized by the local electron gyration radius.

D. Role of electron and ion dynamics

The roles of electron and ion dynamics in the solar wind interaction process are examined by simulation runs that vary mass ratio. The parameters employed in the simulations are summarized in Table II, where series B and C correspond to the variations of ion and electron masses, respectively.

Figure 10(a) shows profiles for the original magnetic field and the induced current density along the equatorial line for series B. The current density profiles resulting from each run are almost identical. This result suggests that the pressure balance between solar wind and magnetosphere, and also the induced current density structure, are determined independently of the ion microscopic dynamics associated with ion mass. The drag coefficient obtained in the steady states from series B is shown in Fig. 11(a) as a function of L/S_i. Additionally, the drag coefficients due to the electron and ion currents, referred to as electron and ion drag coefficients, are plotted in this figure. These drag coefficients are evaluated from a further electromagnetic computation of the ampere force between the coil current density and the electron and ion current densities obtained from the PIC simulation. We have previously established that the electromagnetic simulation for total (ion + electron) current density duplicates the drug coefficient obtained directly from the PIC simulation. The drag coefficients, especially the electron drag coefficient, are almost indistinguishable. The weak dependency of drag coefficient on ion mass comes from the ion drag coefficient. For given magnetosphere scale L/S_e, the ion drag coefficient tends to be negligible small for higher mass ratio.

Figure 10(b) shows profiles for the current density for the runs in series C as a function of L/S_e. This figure clearly shows that the induced current density structure varies according to the electron mass. The obtained drag coefficients are plotted in Fig. 11(b) (asterisk and square dots), together with that resulting from series A (solid and dashed lines). For series C, the electron drag coefficient, which is

TABLE II. Typical dimensionless parameters for simulation series B and C.

Run	L/S_i	L/S_e	m_i/m_e	v_{sw}/v_{ti}	v_{sw}/V_a
B1	0.201	4.26	450	4	2
B2	0.414	4.26	106	4	2
B3	0.852	4.26	25	4	2
C1	0.201	4.26	450	4	2
C2	0.201	2.07	106	4	2
C3	0.201	1.00	25	4	2

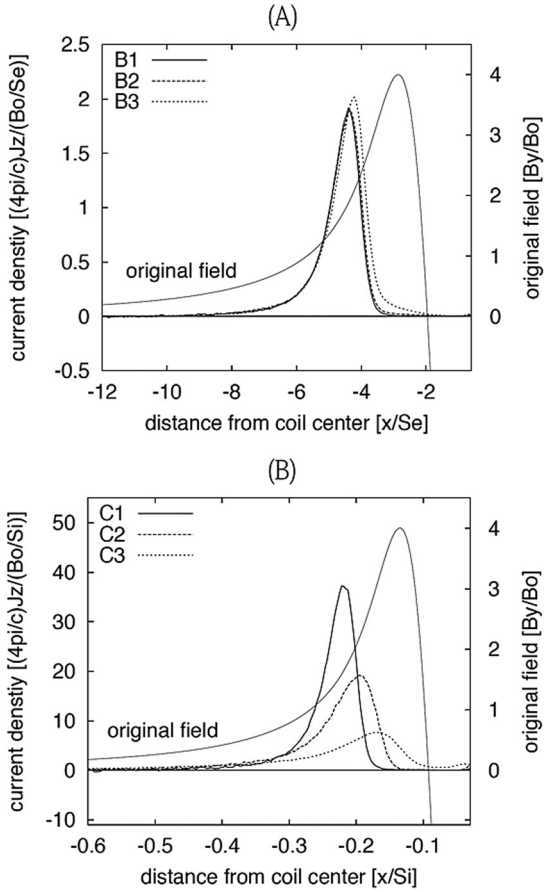

FIG. 10. Profiles of induced current density resulting from series B and C. (a) Solid, dashed, and dotted lines represent profiles for runs B1, B2, and B3, respectively. (b) Solid, dashed, and dotted lines represent profiles for runs C1, C2, and C3, respectively. Profiles of original magnetic field, B_y, are given as solid lines marked "original field."

the dominant component of drag coefficient, increases according to the size of the magnetosphere, similarly to series A. The electron dynamics associated with electron mass, that is, the electron gyration motion[26] is suggested to control mainly the momentum transfer process of solar wind in the small scale magnetospheres under consideration here.

In addition, magnetic field strength at the current density peak is common ($B_y/B_0 \sim v_{SW}/v_a = 2$) for series B and C, as shown in Fig. 10. This concurrency implies that the value of the magnetic field at the front region of the magnetosphere (i.e., the size of the magnetosphere) is primarily determined by the pressure balance, as in the MHD regime, independent of both the electron and ion scale lengths.

E. Scale dependency of drag coefficient

Scale dependency of the drag coefficient is considered based on the induced current density structure. Under the assumption that radius d and internal diameter w of the coil are much smaller than the magnetosphere scale, the coil current density profile $J_z^c(x, y)$ is given by using delta functions $\delta(x, y)$

$$J_z^c(x, y) = C(\delta(x = +d, y = 0) - \delta(x = -d, y = 0)),$$

where C is a coefficient for the current density strength and $d \ll L$. This assumption is valid for realistic hoop coils

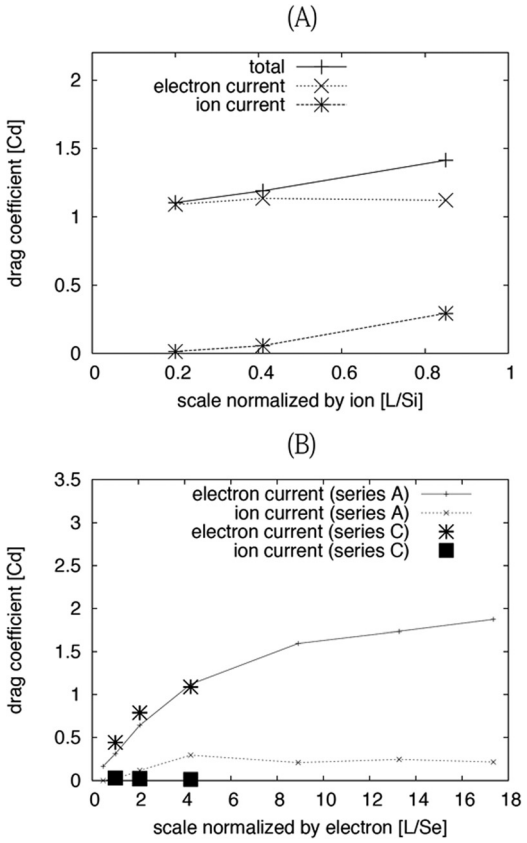

FIG. 11. Scale dependence of drag coefficients. (a) Solid line marked with + represents drag coefficient obtained from series B. Dotted (×) and dashed (∗) lines represent electron and ion drag coefficients, respectively. (b) Dotted lines marked with + and × represent estimated electron and ion drag coefficients obtained from series A, respectively. Electron and ion drag coefficients obtained from series C are denoted by large dots and squares, respectively.

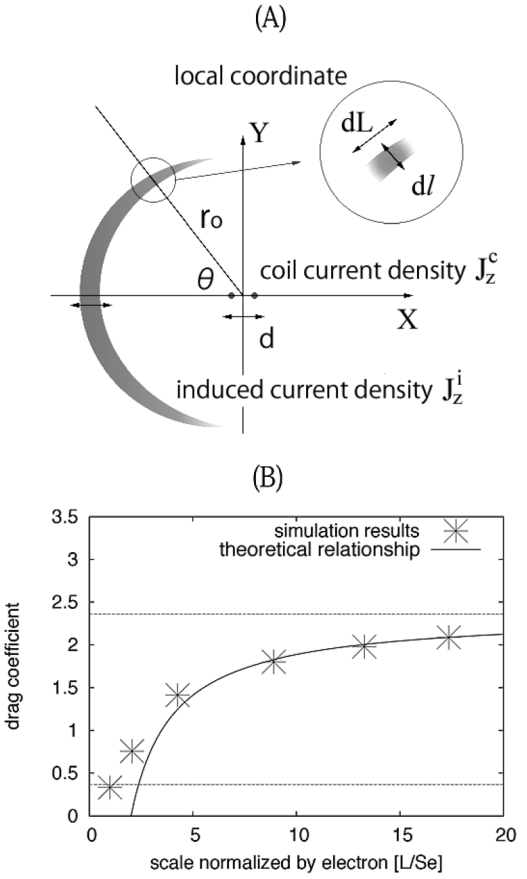

FIG. 12. (a) Schematic diagram for the evaluation of drag coefficient. (b) Drag coefficient as a function of magnetosphere scale obtained from simulation runs A1-A6 (asterisk). Solid line stands for the theoretical relationship (Eq. (15)). Upper and lower horizontal lines represent the limit value of drag coefficient C_d^∞ (Eq. (17)) and the typical value in the small magnetosphere regime (Eq. (16)), respectively.

typically with $d \sim O(1\text{m})$ and $w \sim O(0.1\text{m})$. The Lorentz force F_x^p acting on the coil current is given as

$$F_x^p = \frac{2}{c^2}\int dx_1 dy_1 \int dx_2 dy_2 \frac{J_z^c(x_1,y_1)J_z^i(x_2,y_2)}{|\mathbf{r}|}\cos\theta_0 = \frac{4dC}{c^2}\left(\int dx_2 dy_2 \frac{J_z^i(x_2,y_2)\cos^2\theta}{|\mathbf{r}_0|^2}\right), \quad (7)$$

where J_z^i is induced current density profile and $\mathbf{r} = (x_1 - x_2, y_1 - y_2)$, $\mathbf{r}_0 = (x_2, y_2)$. θ_0 and θ are defined as the angle between x-axis and the vectors $\mathbf{r}$ and $\mathbf{r}_0$, respectively. Schematic diagram for these variables are shown in Fig. 12(a).

The simulation results indicate that the spatial structure of induced current density in the present situation is given by a single-layered current sheet characterized by two factors independently. One is global sheet configuration determined by the pressure balance as in the MHD regime, and the other is local structure at each position of the sheet determined by electron dynamics. We have confirmed that this property of the induced current density is basically satisfied also in the lateral side, except at the vicinity of the pole regions. The difference is that thermal pressure of solar wind, instead of the dynamic pressure, balances with the magnetic pressure in the side region. The induced current density may be given by using global and local coordinates (X, Y) and (dl)

$$J_z^i(x,y)dxdy = J_z^i(X,Y;l)dLdl, \quad (8)$$

where dL is the line element of the global surface of magnetosphere, and dl is the distance from the surface line (see Fig. 12(a)). The integration term in Eq. (7) is then

$$\int dx_2 dy_2 \frac{J_z^i(x_2,y_2)\cos^2\theta}{|r_0|^2} = \int dL \frac{J^g(X,Y)\cos^2\theta}{|r_0|^2}$$
$$J^g(X,Y) \equiv \int dl J_z^i(X,Y;l). \quad (9)$$

Note that r_0 and θ could be defined by the global coordinate. Influence of the local structure on the Lorentz force is included in the function J^g, while the other components relate to the global configuration. The integration term J^g may be approximately estimated by

$$\int dl J_z^i(X,Y;l) \sim C_p(X,Y)W_c(X,Y), \quad (10)$$

where C_p and W_c denote the peak value and half width of current sheet at the global position (X, Y), respectively.

In the case of small coil radius $d \ll L$, the original magnetosphere is regarded as a line dipole magnetic field,[27] which has a homothetic shapes centered at the coils. Since the MHD equations do not include any typical scale lengths, the global configuration of the current layer has a scale-independent similarity for given dynamic and thermal pressures of solar wind. We consider a linear isotropic transform of the configuration corresponding to α times enlargement ($\acute{L} \leftarrow \alpha L$). The similarity of the global configuration indicates that the relevant variables r_0, dL, and θ are transformed as $\acute{r}_0 \leftarrow \alpha r_0$, $\acute{dL} \leftarrow \alpha dL$, and $\acute{\theta} \leftarrow \theta$, respectively. Because the decrease of the line dipole magnetic field is proportional to r^{-2}, corresponding strength of coil current density $\acute{C}$ is $\acute{C} \leftarrow \alpha^2 C$. Thus, the drag coefficient C_d is transformed so as to

$$\acute{C}_d = \frac{\acute{F}^p_z}{2P_{SW}\acute{L}} = \frac{2d\acute{C}}{c^2 P_{SW}\acute{L}} \int \acute{dL} \frac{\acute{J}^g(X,Y)\cos^2\acute{\theta}}{|\acute{r}_0|^2} = \frac{2dC}{c^2 P_{SW} L} \int dL \frac{\acute{J}^g(X,Y)\cos^2\theta}{|r_0|^2}. \tag{11}$$

For the large limit of magnetosphere $\epsilon_p \ll \epsilon_b$,

$$J^g = \frac{c}{8\pi} B_b \equiv J^\infty. \tag{12}$$

In this limit, J^g depends only on the magnetic field to be balanced with the solar wind pressure independently of the scale of the magnetosphere, i.e., $\acute{J}^\infty \leftarrow J^\infty$. Therefore, the drag coefficient for this limit C_d^∞ is scale-independent. According to the peak value and half width of the current layer obtained in Eqs. (3), (4) and (6), the integration terms for the front region in the large and small magnetosphere regimes, J^g_L and J^g_S, are estimated from Eq. (10) as

$$J^g_L(X, Y=0) \sim \left(1 - \frac{\rho_e^L}{\epsilon_b}\right) J^\infty, \tag{13}$$

$$J^g_S(X, Y=0) \sim \left(\frac{v_{ave}}{v_{sw}}\right)^2 \frac{m_e}{m_i + m_e} J^\infty, \tag{14}$$

respectively.

For given solar wind pressure P_{SW} and line dipole magnetic field, the position of pressure balance r_0, corresponding magnetic field B_b, and the dimensionless parameter ρ_e^L/ϵ_b are proportional to P_{SW}^{-1}, $P_{SW}^{1/2}$, and P_{SW}^{-1}, respectively. Therefore, $J^g(X,Y)/|r_0|^2$ increases rapidly as the pressure becomes large. In the case that the dynamic pressure is much larger than the thermal pressure, the integrand in Eq. (11) at the vicinity of the front of the magnetosphere, in which P_{SW} and $\cos^2\theta$ have maximum values, dominantly contributes the integration. Under this assumption, the drag coefficient may be roughly estimated in the same way as the estimation of J^g at the front of the magnetosphere

$$C_d \sim \left(1 - \frac{\rho_e^L}{\epsilon_b}\right) C_d^\infty \quad \text{for } \epsilon_p < \epsilon_b, \tag{15}$$

$$C_d \sim \left(\frac{v_{ave}}{v_{sw}}\right)^2 \frac{m_e}{m_i + m_e} C_d^\infty \quad \text{for } \epsilon_p \geq \epsilon_b. \tag{16}$$

In Fig. 12(b), the theoretical estimation of drag coefficient (Eqs. (15) and (16)) is compared with the simulation results (run A2–A6). The large limit of drag coefficient C_d^∞ (upper horizontal line) is calculated inversely from C_d obtained from run A1

$$C_d^\infty = C_d \frac{C_p^\infty}{C_p}, \quad C_p^\infty \equiv \frac{B_b}{\rho_e^L} \frac{c}{4\pi}. \tag{17}$$

Thus, C_d for run A1 is trivially identical to the theoretical value. The other observed drag coefficients obtained from runs A2–A4 (asterisk) are in agreement with the theoretical scale dependency for large magnetosphere regime (solid line). Also, drag coefficient obtained from runs A5 and A6 approaches to the typical value of small magnetosphere regime (lower horizontal line).

The theoretical relationship obtained here has two features. One is the convergence to a scale-independent limit value in large scale magnetosphere, and the other is drastic decrease appeared in a small magnetosphere with $\epsilon_b \leq \epsilon_p$. In the line dipole magnetic field, $\epsilon_b \leq \epsilon_p$ is equivalent to $L \leq 2\epsilon_p \sim O(\rho_e^L)$. While the former is qualitatively consistent with the scale dependency found in the previous hybrid simulation,[22] the threshold of the decrement is considerably smaller than that reported in the hybrid simulation, $L \sim S_i$. This discrepancy may come from the electrostatic deceleration of ions discussed in the previous sections.

IV. RESULTS UNDER FINITE INTERPLANETARY MAGNETIC FIELD

Simulations that assume a uniform background magnetic field are performed in order to examine the role of IMF in the solar wind interaction process. Background magnetic fields are parallel to the field of the original magnetosphere on the upstream side ($x < 0$), corresponding to the northward IMF in the geomagnetosphere. The strength of the background magnetic field is set as $B_{IMF} = B_b/16$, and the magnetic pressure of the field is negligible compared with the dynamic pressure of solar wind plasma, as in reality. Thus, direct interaction between the background magnetic field and the coil current has little influence on the momentum transfer process.

Figures 13(a) and 13(b) show contour plots for the mass density and out-of-plane magnetic field, respectively. The parameter values used in the simulation, except for the background magnetic field, are the same as those for run A0. A thin peak density region at the front of the magnetosphere and a global out-of-plane magnetic field structure surrounding the magnetosphere are observed as in the zero IMF case (cf. Fig. 3). In addition, magnetic reconnection between the field lines of background magnetic field and magnetosphere takes place near the downstream side of the pole region. Resulting closed field lines are attributed to pile-up inside of the magnetosphere.

Figure 14(a) shows time evolutions for the drag coefficient obtained for finite (solid line) and zero (dotted line)

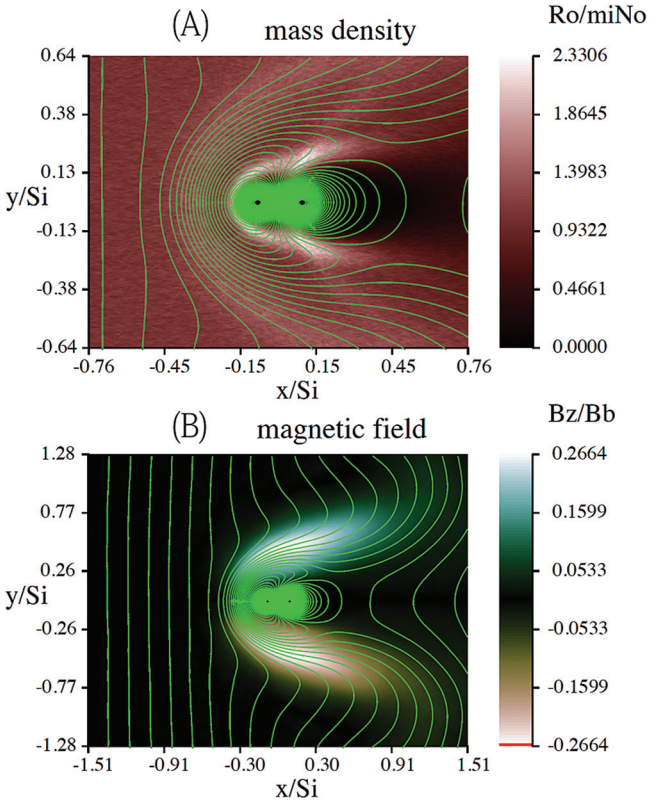

FIG. 13. (Color) (a) Color contours of mass density and (b) out-of-plane magnetic field resulting from finite IMF. Green lines represent magnetic field lines.

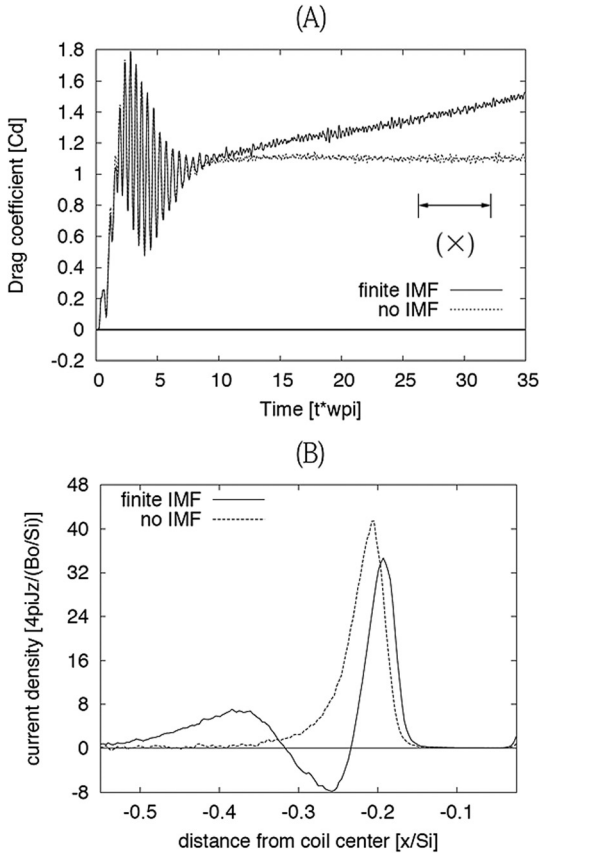

FIG. 14. (a) Time evolution of drag coefficient. Solid and dashed lines denote the drag coefficient resulting from finite and zero IMF cases, respectively. The interval marked by "(×)" is used for time averaging the data in panel (b). (b) Spatial profiles for induced current density resulting from finite (solid line) and zero (dashed line) IMF cases.

IMF. Despite the negligible magnetic pressure, the effects of the IMF are substantial and appear in the momentum transfer process as the time-dependent component of drag coefficient. Profiles for the induced current density along equatorial line ($y = 0$) are given in Fig. 13(b), where solid and dashed lines denote finite and zero IMF, respectively. For finite IMF, the induced current density structure is separated into two layers. The first is formed sharply on the inner side ($|x| < L \sim 0.2S_i$) in comparison to that found for zero IMF. The second is extended widely into the upstream region ($|x| > 0.3S_i$). The induced current density at the inner layer provides a dominant contribution to the Lorentz force.

To clarify the relationship between magnetic reconnection and current density structure, solar wind plasmas are separated into two populations with flags "0" and "1." Plasma particles in the upstream region are designated "1," and once a particle moves through the center line ($x = 0$), its flag is changed to "0." Figure 15 shows number density contour plots for each electron population. The parameter values used to generate the plots are those for run A4 in Table I, except for $B_{IMF} = B_b/16$. Electrons designated "1" are amassed at the front of the closed field lines ($x \sim 1.2S_i > L$) and are distributed away from the coil center. Specifically, solar wind electrons are primary scattered at the surface of the expanded magnetosphere. Conversely, electrons with flag "0" are distributed inside of the closed field lines as well as within the downstream side. This indicates that electrons inside of the magnetosphere travel from the night side through the reconnection region.

Velocity distributions for the electrons (panels (a) and (b)) and for the ions ((c) and (d)) having a flag of "1" are presented in Fig. 16. The vertical and horizontal axes in this figure are the velocity in the x-direction and the distance from the coil center, respectively. The velocity distributions obtained under zero IMF (from run A4) are shown in panels (b) and (d) for comparison. With the zero IMF, ions are gathered at almost the same position as the electron scattering, because of the electrostatic deceleration in this region. Under finite IMF, a difference in the scattered positions of the electrons and ions is evident. While electrons are primary scattered at the front of the extended magnetosphere ($x \sim 1.2S_i$), ions pass through this region and penetrate the magnetosphere. This ion penetration is due to attenuation of the charge separation at the front of the magnetosphere caused by the inner electrons. Instead, electrostatic interaction between ions and inner electrons results in ion scattering inside the magnetosphere ($x \sim 0.5S_i$). The growth of the drag coefficient observed in the finite IMF case originates from the temporal increment of inner electron.

V. SUMMARY AND DISCUSSION

The solar wind interaction and resulting momentum transfer processes for solar wind in a kinetic scale magnetosphere are investigated by 2.5-dimensional full kinetic

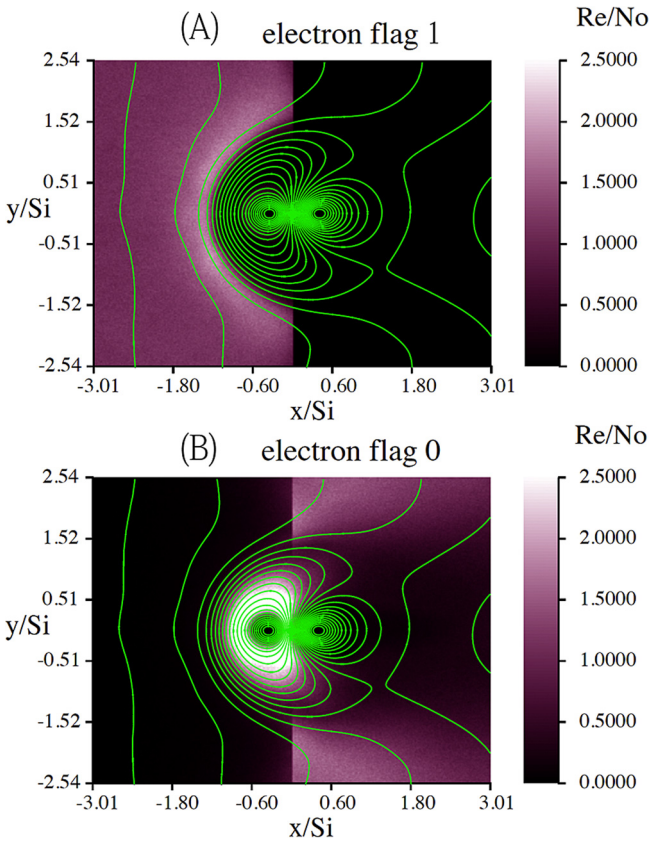

FIG. 15. (Color online) Color-coded contour plots of number density for electrons with (a) A flag of "1," which have not passed through $x = 0$ and (b) A flag of "0," which have passed through $x = 0$. Curved lines in both panels represent magnetic field lines.

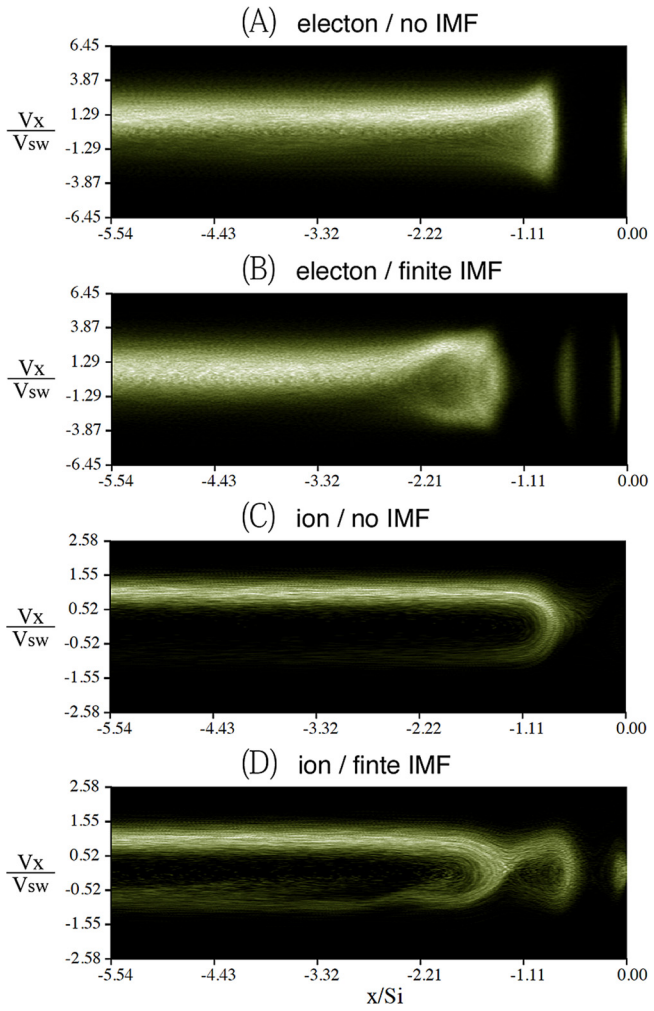

FIG. 16. (Color online) Velocity distribution of electrons and ions with flag "1" along the equatorial line. Vertical and horizontal axes are velocity in the x-direction and distance from coil center, respectively. (a) and (b) Electron velocity distributions obtained under finite and zero IMF, respectively. (c) and (d) Ion distributions obtained under finite and zero IMF, respectively.

particle-in-cell simulations. The spatial scale L of the considered magnetosphere is less than or comparable to the ion inertial length S_i and relevant for magnetized asteroids or spacecrafts with mini-magnetosphere plasma propulsion. The momentum transfer process is considered with respect to the Lorentz force acting on the coil current density, which creates an original magnetosphere. The Lorentz force corresponds to the reaction force of the solar wind scattering. Drag coefficient, C_d, which is defined as the Lorentz force normalized by the solar wind dynamic pressure acting on the typical surface of the magnetosphere, is focused in terms of their dependency on the scale of the magnetosphere.

The solar wind ions, which principally contribute to the solar wind momentum, are decelerated owing to electrostatic interaction with the electrons stagnated at the front of the magnetosphere. As a result of this interaction, the momentum of solar wind can be effectively transferred to the momentum of the coil current density, even for magnetosphere with a small scale of less than the ion inertial length. The corresponding Lorentz force comes from the repulsion between induced current density in out-of-plane direction and the coil current density. In the zero IMF limit, a steady interaction process is observed with a time-independent drag coefficient. Because the out-of-plane current structure is determined by electron gyration radius, obtained drag coefficient for given solar wind dynamic pressure is given as a function of the scale of magnetosphere normalized by the electron gyration radius. For large magnetospheres with $\epsilon_B > \rho_e$, where ϵ_B and ρ_e^L represent gradient scale of original magnetic field and electron gyration radius at the front surface of the magnetosphere, respectively, the drag coefficient increases gradually to an upper limit value C_d^∞ expected for $\epsilon_B \gg \rho_e$ as the scale of the magnetosphere becomes large. When the scale size becomes smaller as $\epsilon_B \leq \rho_e$, the drag coefficient drastically decreases to the typical value $\sim (m_e/m_i)C_d^\infty$.

For the case of finite IMF, the Lorentz force has a time-increment component, and the interaction process does not achieve a steady state. Magnetic reconnection and the resultant electron flow into the magnetosphere play an important role in this interaction process. In addition to the current layer generated at the surface of the magnetosphere, where the solar wind electrons are primarily scattered, an inner current layer is generated due to interaction between inner electrons and incident ions that pass through the surface of the magnetosphere. Even if the strength of IMF is weak enough that the magnetic pressure of IMF is negligible, this process effectively enhances the momentum transfer of solar wind.

Three dimensional flow of solar wind, which is excluded in the present simulation, may also have an impact on the momentum transfer process. Under the influence of some anisotropic scattering mechanisms, solar wind can be diverted in arbitrary directions rather than just in upward/downward direction. The flow direction may be determined so that the drag force acting on the solar wind becomes weak, and the resulting momentum loss of solar wind is expected to be less than that obtained from the two dimensional simulations. Quantitative evaluation of this additional factor remains for future studies. Influence of the three dimensional dynamics of solar wind would be more essential in the finite IMF case with the time-dependent drag coefficient. In this case, saturation of the drag coefficient would depend on the three dimensional election flow inside the magnetosphere, which enables escape of the inner electrons from the magnetosphere to the solar wind through another reconnection site.

The spatial scale of the thin current layer closely relates to the violation mechanism of electron frozen-in constraint. In the present simulation, this constraint is violated by finite orbit effect of electrons expressed by the off-diagonal pressure term. In general, the electron frozen-in constraint could be also violated by the other dissipation mechanisms such as plasma instabilities, collisionless shocks, and so on. The current layer may become thicker than the electron gyration radius under the actions of these mechanisms with larger characteristic scales. In such case, variation of magnetic field gradient and resulting propulsive force tend to become smaller. Some potential dissipation mechanisms, such as bow wave with ion reflection and tearing instability, are hardly found in the small scale magnetosphere with $L < S_i$.[7] Nevertheless, other possibilities to violate electron frozen-in constraint, especially the influence of current driven instabilities that propagates along the induced current direction, are still open questions.

ACKNOWLEDGMENTS

This study was supported by CREST (JST). Computations were performed with the Plasma Simulator at National Institute for Fusion Science and the JAXA Supercomputer System at the Japan Aerospace Exploration Agency. One of the authors (T.M.) acknowledges Professor R. Horiuchi (National Institute for Fusion Science) for useful comments.

[1]A. T. Lui, IEEE Trans. Plasma Sci. **28**, 1854 (2000).
[2]J. A. Slavin, Adv. Space Res. **33**, 1859 (2004).
[3]C. T. Russell, Adv. Space Res. **33**, 2004 (2004).
[4]M. G. Kivelson, J. Warnecke, L. Bennett, S. Joy, K. K. Khurana, J. A. Linker, C. T. Russell, R. J. Walker, and C. Polanskey, J. Geophys. Res. **103**, 19963 (1998).
[5]C. Paty and R. Winglee, Geophys. Res. Lett. **31**, L24806, doi:10.1029/2004GL021220 (2004).
[6]N. Omidi, X. Blanco-Cano, C. T. Russell, H. Karimabadi, and M. Acuna, J. Geophys. Res. **107**, 1487, doi:10.1029/2002JA009441 (2002).
[7]N. Omidi, X. Blanco-Cano, C. T. Russell, and H. Karimabadi, Adv. Space Res. **33**, 1996 (2004).
[8]D. A. Gurnett, J. Geophys. Res. **100**, 21623, doi:10.1029/95JA02225 (1995).
[9]K. Baumgartel, K. Sauer, T. R. Story, and J. F. McKenzie, Icarus **129**, 374 (1997).
[10]E. W. Greenstadt, Icarus **14**, 374 (1971).
[11]N. Omidi, X. Blanco-Cano, C. T. Russell, and H. Karimabadi, Adv. Space Res. **38**, 632 (2006).
[12]N. Omidi, X. Blanco-Cano, and C. T. Russell, J. Geophys. Res. **110**, A12212, doi:10.1029/2005JA011169 (2005).
[13]X. Blanco-Cano, N. Omidi, and C. T. Russell, J. Geophys. Res. **111**, A10205, doi:10.1029/2005JA011421 (2006).
[14]R. M. Zubrin and R. G. Andrews, J. Spacecr. Rockets **28**, 197 (1991).
[15]D. Winske and N. Omidi, Phys. Plasmas **12**, 072514 (2005).
[16]H. Tang and J. Yao, H. Wang, and Y. Liu, Phys. Plasmas **14**, 053502 (2007).
[17]R. M. Winglee, J. Slough, T. Ziemba, and A. Goodson, J. Geophys. Res. **105**, 21067, doi:10.1029/1999JA000334 (2000).
[18]H. Nishida, H. Ogawa, I. Funaki, K. Fujita, H. Yamakawa, and Y. Inatani, AIAA Paper 2005-4463, 2005.
[19]N. Omidi and H. Karimabadi, AIAA Paper 2003–5226, 2003.
[20]Y. Kajimura, D. Shinohara, K. Noda, and H. Nakashima, J. Plasma Phys. **72**, 877 (2006).
[21]G. Khazanov, P. Delamere, K. Kabin, T. J. Linde, and E. Krivorutsky, J. Propul. Power **21**, 853 (2005).
[22]K. Fujita, J. Space Technol. Sci. **20**, 26 (2005).
[23]L. Gargate, R. Bingham, R. Fonseca, R. Bamford, A. Thornton, K. Gibson, J. Bradford, and L. O. Silva, Plasma Phys. Controlled Fusion **50**, 074017 (2008).
[24]H. Yamakawa, I. Funaki, Y. Nakayama, K. Fujita, H. Ogawa, S. Nonaka, H. Kuninaka, S. Sawai, H. Nishida, R. Asahi, H. Otsu, and H. Nakashima, Acta Astronaut. **59**, 777 (2006).
[25]H. Ohtani and R. Horiuchi, Plasma Fusion Res. **4**, 024 (2009).
[26]Dependencies on electron inertial S_e and gyration ρ_e^L scales are indistinguishable in the present simulations with fixed pressure balance because ρ_e^L/S_e is constant. We have also performed another simulation in varying the dynamic pressure (B^b is varied while N_0 is fixed) and confirmed the dominant dependency on the electron gyration radius.
[27]T. Ogino, in *Computer Space Plasma Physics: Simulations and Software*, edited by H. Matsumoto and Y. Omura (TERRAPUB, Tokyo, 1993), p. 161.